Rate and state flow and deformation simulation of microseismicity with elastic emission wavefield synthesis

Matthew D. McChesney, Susan E. Minkoff, George A. McMechan, The University of Texas at Dallas*

Summary

Understanding the flow and deformation that occurs in a reservoir during fluid injection for enhanced oil and gas recovery is critical for maximizing the efficiency of production from unconventional reservoirs. A one-way coupled model for flow and deformation simulation is used for microseismic nucleation and subsequent wavefield modeling of the elastic emissions from the microseismic events.

Introduction

In unconventional reservoirs (e.g. organic rich shales, tight sandstones, or chalks) low porosity and permeability inhibit fluid flow through the matrix to a producing well. Fluid and proppant injection at high pressures leads to reactivation of in situ fractures and the generation of new hydraulic fractures. These fractures provide high permeability conduits to the well, thus allowing viable production from otherwise unproducible formations. Quantifying the extent and type of this deformation helps to define the drainage capability of a well and thus the production potential. Useful techniques for quantifying this deformation include numerical modeling of flow and deformation and of microseismic monitoring of the injection (see Maxwell et al., 2015).

Models from flow and deformation simulation can help to quantify the range of potential reservoir responses through sensitivity analyses. The range of possible deformation results from numerical modeling (from only minor variations to the model parameters) is well documented by McClure and Horne (2011) and Gischig (2015). Large variations in the modeled deformation response of the reservoir were observed from only small perturbations to the fluid injection parameters and to the in situ fracture geometries and stress regimes. Attempts to constrain the geomechanics in the face of this uncertainty include the work of Baig, et al., 2015.

Monitoring of microseismicity can provide a direct measure of reservoir deformation during fluid injection (see, for example, Rodriguez-Pradilla, 2015). Location of microseismic events via analysis of the elastic emissions recorded during injection can quantify the extent of the deformed reservoir (Majer and Doe 1986; Maxwell and Cipolla, 2011). Focal mechanism analyses of the microseismic events can quantify the type of deformation that has occurred (Urbancic et al., 1993). In practice, the quantification of deformation in the reservoir via microseismic monitoring is often limited by uncertainty in the velocity structure through which the elastic emissions are traveling, the limited aperture of the monitoring arrays, and the ambiguity in the fault plane solution of the focal mechanism analysis.

To provide a context in which flow and deformation simulation results can be better constrained via elastic emission analysis and in which elastic emissions may be better understood with respect to the flow and deformation in the reservoir, it is desirable to model both the flow and deformation and the resulting elastic emissions. Below we outline a method for sequential modeling of flow and deformation in a 2D elastic medium with 1D fractures followed by 3D visco-elastic seismic modeling of the resulting elastic emissions. The modeling shown demonstrates expected behaviors for microseismic event nucleation with respect to the flow and deformation in the reservoir and appropriate elastic emission radiation patterns in the synthetic seismograms for the simulated microseismic events.

Theory and implementation

The flow and deformation simulation is performed using the Complex Fracturing ReseArch Code (CFRAC). CFRAC is an open source code that was originally developed by McClure and Horne at Stanford University (McClure, 2012). Wavefield simulation is performed using code developed at The Center for Lithospheric Studies at The University of Texas at Dallas (see Ramos-Martinez et al. (2003)).

We examine flow and deformation modeling along fractures embedded in a 2D homogenous, isotropic, elastic medium by implementation of a rate and state treatment of frictional sliding along the fractures. The single-phase fluid flow is confined to preexisting and predefined hydraulic fractures and is modeled via a 1D finite volume method (Karimi-Fard et al., 2004). Deformation and the resulting induced stress perturbation in the medium surrounding the fractures are calculated via the displacement discontinuity implementation of the boundary element method (Shou and Crouch, 1995). To achieve a more realistic treatment of the frictional sliding along the fractures for modeling microseismicity, the rate and state friction law is employed. For the rate and state friction law,

the coefficient of friction is dependent on the material parameters f_0, v_0, a, b, and d_c, and on the sliding velocity v, and the state (sliding history) variable θ, of the sliding fracture (Segall, 2010):

$$\mu_f = f_0 + a\ln\left(\frac{v}{v_0}\right) + b\ln\left(\frac{\theta v_0}{d_c}\right) \quad (1)$$

where f_0 is a constant reference value for the coefficient of friction, v_0 is a constant reference velocity, d_c is a characteristic slip distance, and a and b are empirically derived coefficients. The state variable, θ, can be thought of as the evolving average asperity contact time across the sliding fracture (Segall, 2010):

$$\frac{\partial\theta}{\partial t} = 1 - \frac{\theta v}{d_c} \quad (2)$$

The coupling of flow and deformation is achieved iteratively. In each iteration the shear displacements are solved for first followed by the pressure and normal displacements. (Kim et al., 2011; McClure, 2012). Microseismic events are defined to occur on any given element of the fracture when the sliding velocity of that element exceeds a user-defined minimum velocity. These events are assumed to have ended when the sliding velocity falls back below an additional user defined threshold.

Forward wavefield modeling of the resulting elastic microseismic emissions is performed via finite-difference modeling. An eighth-order in space and second-order in time finite-difference scheme for the velocity-stress formulation of the wave equation is implemented on a staggered grid. The equations of motion and constitutive equations are defined as in Robertson et al. (1994). The numerical simulator for the wave equation solution supports modeling through a 3D, heterogeneous, viscoelastic medium. However, in this work the domain for our wavefield modeling is parameterized to be homogenous, isotropic, and effectively elastic in accordance with the medium requirements for the flow and deformation simulation. The fractures in the flow and deformation simulation are embedded in this homogenous, background medium. Given that the fracture widths in this parameterization are significantly less than the seismic scale and that the fluid flow is restricted to the fractures, the medium for the wavefield propagation is defined without explicit inclusion of the fractures. Microseismic sources are extracted from the flow and deformation simulation and injected into the wavefield modeling solution as moment tensors parameterized via strike, dip, and rake (Graves (1996)).

Each experiment is composed of two parts: 1) the flow and deformation simulation including generation of simulated microseismic events by the rate and state method, followed by 2) a forward solve of the wave equation using the simulated microseismic events as sources for the wave equation, and construction of seismograms via sampling of the propagating wavefield at defined receiver locations.

Numerical results

The numerical results for two models are presented below. The homogeneous background does not require gridding for the flow and deformation simulation as the displacement discontinuity boundary element method (BEM) is employed for derivation of the stress perturbations away from the fractures. However, a 2 x 2 m grid is used to display the stress perturbation and for the wavefield modeling. To produce synthetic seismograms from the propagating wavefield, two 1D arrays of virtual seismometers are embedded in the homogenous background medium (Figure 1).

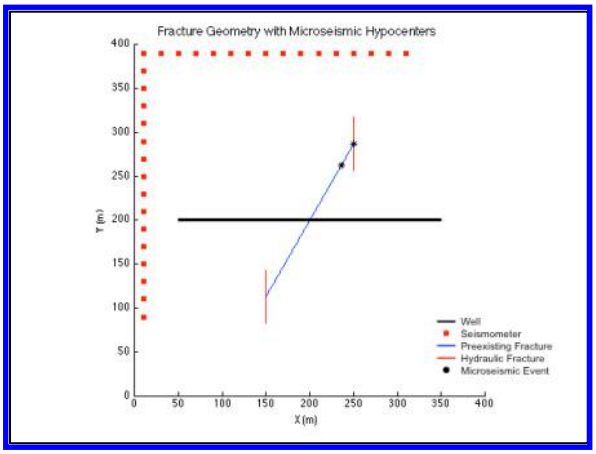

Figure 1: Flow and deformation and wavefield modeling domain including injection wellbore and receiver arrays, and fracture geometries for Model a and 2. Locations of microseisms 65 and 61 are shown.

The flow and deformation simulations and wavefield modeling are performed on two predefined fracture geometries, Model 1 and Model 2. Model 1 contains a single preexisting fracture that intersects the wellbore and is inclined to it at an angle of ~60° (see Figure 1). Model 2 includes the same preexisting fracture with the addition of two potentially-forming, hydraulic fractures that extend for ±30 m from the fracture tips of the preexisting fracture in a direction parallel to the y-axis (Figure 1). The choice of fracture orientations is defined in agreement with any expected fracture opening consistent with the far-field stress state. The maximum and minimum far-field horizontal stresses for both models are parallel to the x and y-axes and are defined to be $\sigma_{hmax} = \sigma_{yy} = 100$ MPa and $\sigma_{hmin} = \sigma_{xx} = 60$ MPa. Thus the expected opening direction for hydraulic fractures is parallel to the x-axis which agrees with the orientations of the two potentially-forming, hydraulic fractures in Model 2.

The flow and deformation simulation consists of fluid injection into the wellbore at constant pressure, P_{inj} = 60 MPa, and a variable injection rate with a maximum of q_{inj} = 80 kg/s. The wellbore is open to the formation and thus fluid flow occurs directly into the preexisting fracture. Injection is performed for 3600 s. Two flow and deformation simulations (1 and 2), including microseismic event generation via the rate and state method are run on Models 1 and 2 respectively with the same simulation parameters (see Table 1).

Simulation Parameters		
P_{init}	Initial pressure in fractures	40 MPa
t_{max}	Max simulation time	3600s
P_{inj}	Max injection pressure	70 MPa
q_{inj}	Max injection rate	80 kg/s
μ	Fluid viscosity	1 cp
S_0	Cohesion of close elements	0.5 MPa
$S_{0,open}$	Cohesion of open elements	0.5 MPa
E_0	Void aperture reference value	0.0005 m
e_0	Hydraulic aperture reference value	0.0005 m
σ_{yy}	Far-field normal stress in y-direction	100 MPa
σ_{xx}	Far-field normal stress in x-direction	60 MPa
σ_{yy}	Far-field shear stress in xy-direction	0 MPa
G	Shear modulus of background medium	15625 MPa
ν	Poisson's ratio of background medium	0.2576
ρ	Bulk density of background medium	2500 kg/m^3
Q_p	P-wave quality factor	10000
Q_s	S-wave quality factor	10000
Rate and State Parameters		
f_0	Reference coefficient of friction	0.6
a	Velocity effect coefficient	0.01
b	State effect coefficient	0.015
d_c	Characteristic slip distance	0.05 mm
v_0	Reference velocity	1e^{-6} m/s

Table 1: Flow and deformation simulation and wavefield modeling parameters.

In Simulations 1 and 2, a microseismic event is defined to be initiated when the sliding velocity along the fracture exceeded 5 mm/s and to have ended when the sliding velocity dropped back below 2.5 mm/s. The flow and deformation simulations in both models result in episodic evolution of the injection rate and microseismicity associated with slip and opening at the tips of the open portion of the fractures. Figure 2 shows the evolution of injection rate with time for Simulation 1 with the magnitudes of the resulting microseismic events displayed at their corresponding initiation times. Periods of decreasing injection rate proceed with rapid failure at the tips of the fractures resulting in nucleation of microseismic events. This is followed by spikes in the injection rate associated with the creation of new void space where the open portion of the fractures has been extended thus causing an increase in injection rate at constant pressure. Figure 3 illustrates the temporal relationship between the microseismic event initiation times and the changes in injection rate.

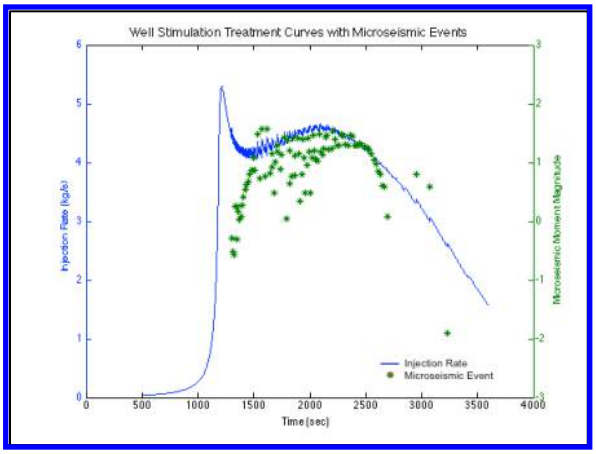

Figure 2: Injection rate vs time for Simulation 1 with asscociated microseismicity.

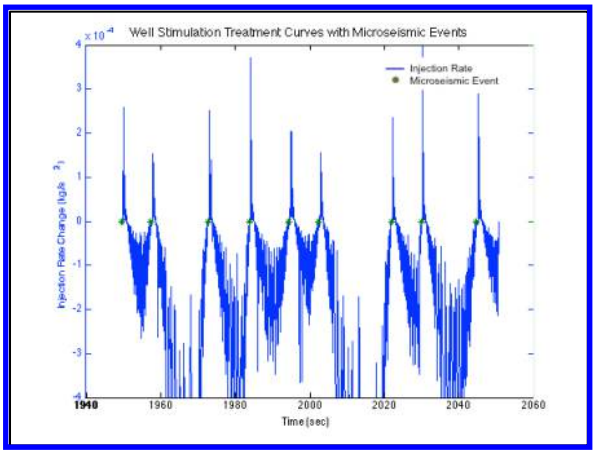

Figure 3: Change in injection rate vs time with microsesmic event onset times from 1950-2050 s of Simulation 1.

Following the flow and deformation simulation two microseismic events are extracted and injected as moment tensor sources for viscoelastic wavefield modeling of elastic emissions. Figure 1 shows the location of two microseismic events extracted from Simulation 2; microseism 65 which is located on the preexisting vertical fracture which has a strike of ~60° to the x-axis, and microseism 61 which is located on the new hydraulic fracture that has formed during the flow and deformation simulation. The vertical hydraulic fracture has a strike of 90° to the x-axis and the sense of slip is determined by the deformation simulation. Figures 4 and 5 show the v_x and v_y components for the particle velocity field as recorded on the two arrays of virtual seismometers for the two microseismic events considered. The upper image in each figure corresponds to microseism 61 and the lower to microseism 65.

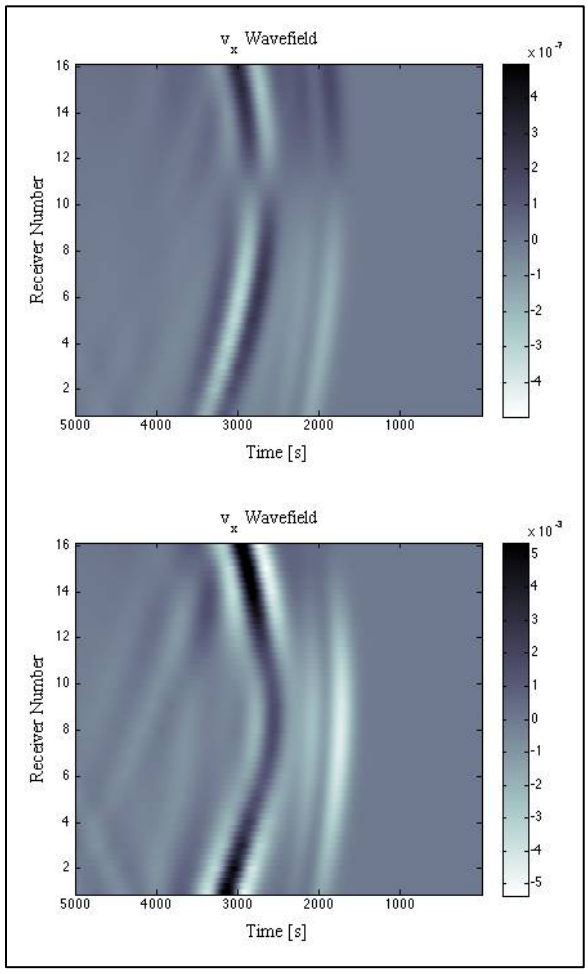

Figure 4: X-component of particle velocity for microseisms 61 and 65 as recorded on array oriented parallel to the y-axis.

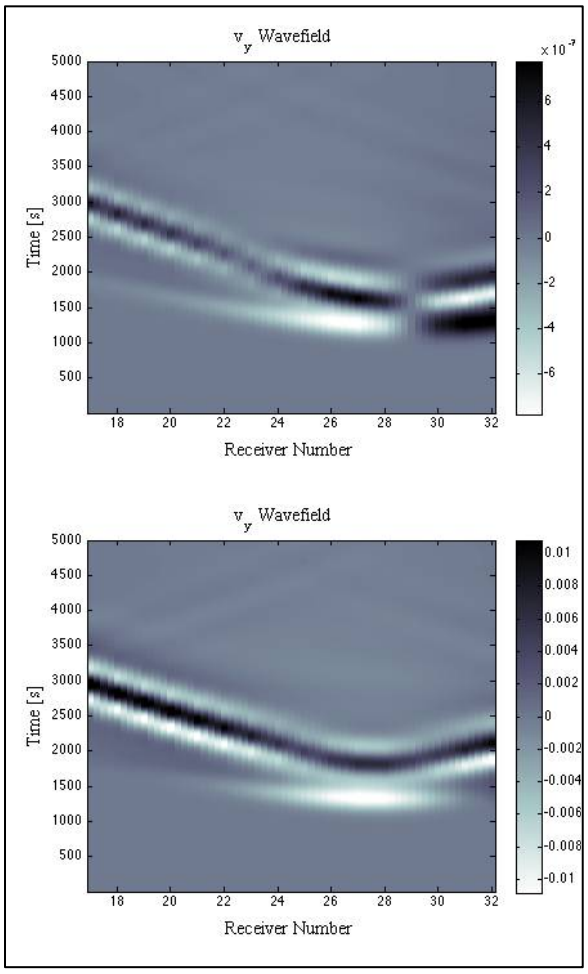

Figure 5: Y-component of particle velocity for microseisms 61 and 65 as recorded on array oriented parallel to the x-axis.

The polarities of the P-wave direct arrivals on the two arrays reflect the differences in radiation pattern for the two microseismic events as governed by the associated failure geometries. In Figure 4 the x-component of the particle velocity associated with the P-wave direct arrivals for microseism 61 shows the expected polarity reversal about receiver 11 corresponding to the anti-nodal plane. The polarity reversal about the nodal plane for microseism 61 is observed on the y-component of the particle velocity for the P-wave in Figure 5. For microseism 65 the nodal and anti-nodal planes of the elastic emissions are oriented such that the polarity reversal falls of the ends of the arrays, and a direct arrival of consistent polarity for the particle velocities associated with the P-wave is observed on both arrays.

Conclusions

Numerical modeling of flow and deformation and microseismic monitoring provide two tools for quantifying deformation in the reservoir during fluid injection. We present a one-way coupled approach to modeling flow and deformation with microseismic event simulation via the rate and state treatment of frictional sliding followed by elastic emission seismic modeling. The observed model responses for microseismicity in the context of the flow and deformation simulation and the elastic emission radiation patterns for the known microseismic sources are confirmed.

Acknowledgments

The research leading to this paper was supported by Pioneer Natural Resources, and by the sponsors of the UT-Dallas Geophysical Consortium.

EDITED REFERENCES

Note: This reference list is a copyedited version of the reference list submitted by the author. Reference lists for the 2016 SEG Technical Program Expanded Abstracts have been copyedited so that references provided with the online metadata for each paper will achieve a high degree of linking to cited sources that appear on the Web.

REFERENCES

Baig, A., G. Viegas, J. Gallagher, T. Urbancic, and E. von Lunen, 2015, Constraining geomechancial models by using microseismic-derived fractures from source mechanisms: The Leading Edge, **34**, 912–916, http://dx.doi.org/10.1190/tle34080912.1.

Gischig, V. S., 2015, Rupture propagation behavior and the largest possible earthquake induced by fluid injection into deep reservoirs: Geophysical Research Letters, **42**, 7420–7428, http://dx.doi.org/10.1002/2015GL065072.

Graves, R. W., 1996, Simulating seismic wave propagation in 3D elastic media using staggered-grid finite differences: Bulletin of the Seismological Society of America, **86**, 1091–1106.

Karimi-Fard, M., L. J. Durlofsky, and K. Aziz, 2004, An efficient discrete-fracture model applicable for general purpose reservoir simulators: SPE Journal, **9**, http://dx.doi.org/10.2118/88812-PA.

Kim, J., H. A. Tchelepi, and R. Juanes, 2011, Stability, accuracy, and efficiency of sequential methods for coupled flow and geomechanics: SPE Journal, **16**, http://dx.doi.org/0.2118/119084-PA.

Majer, E. L., and Doe, T. W., 1986, Studying hydrofractures by high frequency seismic monitoring: International Journal of Rock Mechanics and Mining Sciences & Geomechanics Abstracts, **23,** 185–199, http://dx.doi.org/10.1016/0148-9062(86)90965-4.

Maxwell, S. C., and Cipolla, C. L., 2011, What does microseismicity tell us about hydraulic fracturing? SPE Annual Technical Conference and Exhibition, SPE.

Maxwell, S. C., D. Chorney, and S. D. Goodfellow, 2015, Microseismic geomechanics of hydraulic-fracture networks: Insights into mechanisms of microseismic sources: The Leading Edge, **34**, 904–910, http://dx.doi.org/10.1190/tle34080904.1.

McClure, M., 2012, Modeling and characterization of hydraulic stimulation and induced seismicity in geothermal and shale gas reservoirs: Ph.D. thesis, Stanford University.

McClure, M. W., and R. N. Horne, 2011, Investigation of injection-induced seismicity using a coupled fluid flow and rate/state friction model: Geophysics, **76**, no. 6, WC181–WC198, http://dx.doi.org/10.1190/GEO2011-0064.1.

Ramos-Martinez, J., G. A. McMechan, and M. Dillen, 2003, Documentation of software for 3-D eighth-order staggered-grid finite-difference seismic modeling in viscoelastic media, The UT-Dallas Geophysical Consortium, Center for Lithospheric Studies, The University of Texas.

Robertsson, J. O., J. O. Blanch, and W. W. Symes, 1994, Viscoelastic finite-difference modeling: Geophysics, **59**, 1444–1456, http://dx.doi.org/10.1190/1.1443701.

Rodriguez-Pradilla, G., 2015, Microseismic monitoring of a hydraulic-fracturing operation in a CBM reservoir: Case study in the Cerrejon Formation, Cesar-Rancheria Basin, Columbia: The Leading Edge, **34**, 896–902, http://dx.doi.org/10.1190/tle34080896.1.

Segall, P., 2010, Earthquake and volcano deformation: Princeton University Press.

Shou, K. J., and S. L. Crouch, 1995, A higher order displacement discontinuity method for analysis of crack problems, International Journal of Rock Mechanics and Mining Sciences and Geomechanics Abstracts, **32**, 49–55, http://dx.doi.org/10.1016/0148-9062(94)00016-V.

Urbancic, T. I., Trifu, C. I., and Young, R. P., 1993, Microseismicity derived fault-planes and their relationship to focal mechanism, stress inversion, and geologic data: Geophysical Research Letters, **20**, 2475–2478, http://dx.doi.org/10.1029/93GL02937.